XUV Absorption by Solid Density Aluminum

C. A. Iglesias

September 30, 2009

High energy density physics

Disclaimer

This document was prepared as an account of work sponsored by an agency of the United States government. Neither the United States government nor Lawrence Livermore National Security, LLC, nor any of their employees makes any warranty, expressed or implied, or assumes any legal liability or responsibility for the accuracy, completeness, or usefulness of any information, apparatus, product, or process disclosed, or represents that its use would not infringe privately owned rights. Reference herein to any specific commercial product, process, or service by trade name, trademark, manufacturer, or otherwise does not necessarily constitute or imply its endorsement, recommendation, or favoring by the United States government or Lawrence Livermore National Security, LLC. The views and opinions of authors expressed herein do not necessarily state or reflect those of the United States government or Lawrence Livermore National Security, LLC, and shall not be used for advertising or product endorsement purposes.

XUV absorption by solid density aluminum

CARLOS A. IGLESIAS

Lawrence Livermore National Laboratory,
PO Box 808, Livermore, CA 94550 USA

Abstract

An inverse bremsstrahlung model for plasmas and simple metals that approximates the cold, solid Al experimental data below the L-edge is applied to matter conditions relevant to XUV laser applications. The model involves an all-order calculation using a semi-analytical effective electron-ion interaction. The predicted increases in XUV absorption with rising temperature occur via two effects: increased availability of final states from reduced electron degeneracy and a stronger electron-ion interaction from reduced screening. Discrepancies in the temperature dependence as well as other details between the present approach and a recently proposed absorption model are discussed.

Corresponding author:

Tel.: (925) 422-7252

Fax: (925) 423-7228

E-mail address: iglesias1@llnl.gov

1. Introduction

Recently Vinko et al [1] (hereafter VGW) observed that free-electron lasers offer an excellent opportunity to study the opacity of warm dense Al. One complication is eliminated since the heating is fast and hydrodynamic motion does not play an important role. Furthermore, theory often separates photon absorption contributions and inverse bremsstrahlung dominates the XUV Al opacity below the L-edge; thus, isolating a single process.

Several authors have studied photon absorption by electron fluids. [1,2] Nevertheless motivated by the renewed interest, Al absorption calculations relevant to free-electron laser applications using a moderately simple model are presented. Inverse bremsstrahlung is briefly reviewed in Sect. 2 and the model, which is based on standard concepts, is introduced in Sect. 3. Results and comparisons to experimental data are presented in Sect. 4 with an analysis in Sect. 5. The VGW results are discussed in Sect. 6 followed by conclusions in the last section.

2. Inverse Bremsstrahlung

The non-relativistic, thermally averaged inverse bremsstrahlung extinction coefficient of a photon with energy $\hbar\omega$ by an isolated electron-ion pair is often written in the form [3]

$$\alpha_{IB}(\omega) = g(\omega,T)\alpha_K(\omega) \tag{2.1}$$

with T the temperature in energy units. The thermally averaged Gaunt factor, $g(\omega,T)$, accounts for quantum mechanical corrections to the classical Kramers result, $\alpha_K(\omega)$. [4]

2.1 Collective effects

Equation (2.1) assumes that electron-ion pairs are independent. Collective phenomena, however, alter the absorption by screening the electron-ion interaction. [5-8] Furthermore, degeneracy modifies the thermal average so that [8]

$$g(\omega,T) = \frac{\sqrt{\pi}}{2I_{1/2}(\eta)} \int_o^\infty \frac{d\varepsilon}{T} f_\eta\left(\frac{\varepsilon}{T}\right)\left[1 - f_\eta\left(\frac{\varepsilon + \hbar\omega}{T}\right)\right]g(\varepsilon,\omega) \tag{2.1.1}$$

where the Fermi-Dirac distribution and Fermi integrals are defined as

$$f_\eta(x) = \left(1 + e^{x-\eta}\right)^{-1} \tag{2.1.2}$$

$$I_\mu(\eta) = \frac{1}{\Gamma(1+\mu)} \int_o^\infty dx\, x^\mu f_\eta(x) \tag{2.1.3}$$

with η the chemical potential divided by T and $\Gamma(x)$ the Gamma function. [9]

The Gaunt factor $g(\varepsilon,\omega)$ with ε the initial electron energy is usually computed in the one-electron picture. The calculations are often performed in the dipole approximation and partial wave decomposition leads to [3]

$$g(\varepsilon,\omega) = \frac{\sqrt{3}}{2\pi\sqrt{\varepsilon(\varepsilon + \hbar\omega)}} \sum_{\ell=1}^{\infty} \ell\left\{M_{\ell,\ell-1}^2(\varepsilon,\omega) + M_{\ell,\ell+1}^2(\varepsilon,\omega)\right\} \tag{2.1.4}$$

The dipole matrix element is most readily evaluated in the "acceleration" form,

$$M_{\ell,\ell'}(\varepsilon,\omega) = \int_o^{\infty} dr \psi_{\varepsilon\ell}(r) \frac{dV_s(r)}{dr} \psi_{\varepsilon+\hbar\omega,\ell'}(r) \tag{2.1.5}$$

where $\psi_{\varepsilon\ell}(r)$ is the electron wave function with energy ε and orbital angular momentum ℓ, moving in the spherically symmetric potential $V_s(r)$ with outgoing wave boundary conditions.

The static potential is determined by an average charge distribution of the ion. For example,

$$V_s(r) = V_b(r) - \frac{Ze^2}{r}e^{-r/\lambda} \tag{2.1.6}$$

with Ze the net ion charge, λ a many-body screening length, and $V_b(r)$ a short-ranged, frozen-core potential due to bound electrons so that $V_s(r \to 0) = -Z_N e^2/r$ with $Z_N e$ the nuclear charge.

2.2 Dispersion and multiple collisions

In addition, there are dispersion and multiple collisions that can impact the absorption for photon frequencies near and below the plasmon resonance. [7,10] The Drude model approximates these effects with a complex refractive index of the form [10]

$$N^2(\omega) = 1 - \frac{\omega_p^2}{\omega[\omega + i\nu(\omega)]} \tag{2.2.1}$$

where $\nu(\omega)$ is a collision frequency and $\omega_p = \sqrt{4\pi e^2 n/m}$ with n and m the electron free number density and mass, respectively. The resulting absorption and index of refraction are [10]

$$\alpha_D(\omega) = \frac{2\omega}{c}\text{Im}N(\omega) = \frac{\omega_p^2}{\omega^2 + \nu^2(\omega)}\frac{\nu(\omega)}{n(\omega)c} \tag{2.2.2}$$

$$n(\omega) = \text{Re}\,N(\omega) = \sqrt{\frac{\omega\left(\omega^2 - \omega_p^2 + \nu^2\right) + \sqrt{\left(\omega^2 + \nu^2\right)\left(\omega^2 - \omega_p^2\right)^2 + \omega^2\nu^2}}{2\omega\left(\omega^2 + \nu^2\right)}} \tag{2.2.3}$$

where c is the speed of light in vacuum.

2.3 Born approximation

Systematic derivations of the inverse bremsstrahlung cross-section in a fluctuating medium lead to second-order expressions of the energy dependent Gaunt factor, [5-7]

$$g^{(2)}(\varepsilon,\omega) = \frac{\sqrt{3}}{\pi} \int_{k_-}^{k_+} \frac{dq}{q} S(q) \frac{F^2(q)}{|D(q,\omega)|^2} \tag{2.3.1}$$

where $F(q)$ is simply related to the Fourier transform of the unscreened electron-ion interaction,

$$F(q) = \frac{q^2}{4\pi e^2} \int d\vec{r} e^{i\vec{q}\cdot\vec{r}} V(r) \tag{2.3.2}$$

and

$$\frac{\hbar^2 k_\pm^2}{2m} = 2\varepsilon + \hbar\omega \pm 2\sqrt{\varepsilon(\varepsilon + \hbar\omega)} \tag{2.3.3}$$

define the maximum and minimum wave number momentum transfer. This expression for the energy dependent Gaunt factor includes dynamic screening and ion-ion correlations through the plasma dielectric function, $D(q,\omega)$, and the ion structure factor, $S(q)$, respectively.

The results in Eq. (2.1.4) simplify in the Born approximation to [3]

$$g_{Born}(\varepsilon,\omega) = \frac{\sqrt{3}}{\pi} \int_{k_-}^{k_+} \frac{dq}{q} F_s^2(q)$$

$$= \frac{\sqrt{3}}{\pi} \int_{k_-}^{k_+} \frac{dq}{q} F_b^2(q) + Z^2 g_{Born}^\lambda(\varepsilon,\omega) \tag{2.3.4}$$

with $F_s(q)$ and $F_b(q)$ related to the Fourier transform of $V_s(r)$ and $V_b(r)$, respectively, and

$$g_{Born}^\lambda(\varepsilon,\omega) = \frac{\sqrt{3}}{2\pi} \left\{ \ln\left[\frac{1 + \lambda^2 k_+^2}{1 + \lambda^2 k_-^2}\right] + \frac{1}{1 + \lambda^2 k_+^2} - \frac{1}{1 + \lambda^2 k_-^2} \right\} \tag{2.3.5}$$

where Eq. (2.1.6) was used to get the last line of Eq. (2.3.4). One difference between Eq. (2.3.1) and (2.3.4) is dynamic rather than static screening of the interaction. The second difference is the absence of ion-ion correlations in the latter. Both are considered in Sect 5.

3. Proposed Model

An approximation for the collision frequency can be obtained by comparing Eq. (2.1) and Eq. (2.2.2) for large photon frequencies for which $n(\omega) \approx 1$ and $\nu(\omega) << \omega$, to yield

$$\frac{v(\omega)}{c} = \frac{\omega^2}{\omega_p^2} g(\omega,T)\alpha_K(\omega) \tag{3.1}$$

The proposed *ad hoc* model for the photon absorption assumes the form in Eq. (2.2.2) corrected for stimulated emission,

$$\alpha(\omega) = \left(1 - e^{-\hbar\omega/T}\right)\frac{\omega_p^2}{\omega^2 + v^2(\omega)}\frac{v(\omega)}{n(\omega)c} \tag{3.2}$$

with $v(\omega)$ and $n(\omega)$ in Eqs. (3.1) and (2.2.3). The model incorporates many of the essential phenomena in inverse bremsstrahlung for plasmas and simple metals. [11]

The input to the model is the static potential. Here, the form in Eq. (2.1.6) is kept and use the analytic potential designed to reproduced atomic data of isolated ions with accuracy comparable to single configuration, relativistic, self-consistent-field calculations. [12] Thus, the potential reasonably describes the average charge distribution of a nucleus plus bound electrons. The many-body screening of the long-ranged Coulomb tail from the net ion charge assumes

$$\lambda = \sqrt{\frac{T}{4\pi e^2 n_e}\frac{I_{1/2}(\eta)}{I_{-1/2}(\eta)}} \tag{3.3}$$

which is a generalized electron Debye length. [13] The degeneracy parameter is obtained assuming an ideal electron gas,

$$n\lambda_T^3 = 2I_{1/2}(\eta) \tag{3.4}$$

where $\lambda_T = \sqrt{2\pi\hbar^2/mT}$ is the thermal de Broglie wavelength.

4. Results

The *L*-shell electrons in thermal equilibrium, solid-density Al are not expected to ionize significantly until the temperature is above ~10eV. [1] The model electron-ion interaction is then given by $Z = 3$ and frozen-core potential,

$$V_b(r) = -\frac{e^2}{r}\left[2e^{-r/\lambda_K} + 8e^{-r/\lambda_L}\right] \tag{4.1}$$

where $\lambda_K = 0.1009a_o$ and $\lambda_L = 0.3752a_o$ with a_o the Bohr radius. [12]

4.1 Cold aluminum

Absorption data for cold, solid Al is commonly quoted from two sources [14,15] that disagree below the *L*-edge. Recent measurements, however, agree with the earlier data; thus, it is

taken as the more accurate. [1,16] The Al photon absorption from the present model at $T = 0.025 eV$ and measurements [14] are presented in Fig. 1 (the calculation with $V_b(r) = 0$ is discussed in Sect. 5 and those from VGW in Sect. 6). The degeneracy and screening parameter in the calculation are provided in Table 1 and the matrix elements in Eq. (2.1.5) were computed using the phase-amplitude method. [17] For these short ranged potentials, however, the Green's function approach [18] should not be significantly more time consuming. The figure shows reasonable agreement between the present model and experimental data (e.g.; earlier comparisons show larger discrepancies [1,19]).

Index of refraction calculations for cold, solid Al are displayed in Fig. 2 showing good agreement with the measurements. [20,21] The figure includes the high frequency approximation (collisionless plasma, $v = 0$),

$$n_o(\omega) = \sqrt{1 - \frac{\omega_p^2}{\omega^2}} \qquad (4.1.1)$$

valid for $\omega > \omega_p$ and in reasonable agreement with the model above the plasma frequency. The figure also explains the sharp increase in absorption below the plasma frequency as a consequence of the decrease in the index of refraction. Finally, note the discrepancy at small photon energies due in part to neglected ion-ion correlations discussed in Sect. 5.

4.2 Warm aluminum

Given the reasonable success of the model in reproducing the cold Al data, it is tempting to try warmer conditions accessible with free-electron laser experiments. The ratios of absorption calculations at several temperatures to the $T = 0.025 eV$ result are plotted in Fig. 3 with input degeneracy and screening parameter given in Table 1. The figure shows decreased absorption for $\omega < \omega_p$ caused in part by the behavior of the index of refraction. For example, displayed in Fig. 2 are calculations for solid-density Al at $T = 10 eV$ showing the temperature behavior of $n(\omega)$. The enhanced absorption for $\omega > \omega_p$ with increasing temperature is due to changes in screening length and degeneracy.

The longer screening length strengthens the electron-ion interaction increasing the collision frequency (shape resonances can produce exceptions [18]). Note that although there is a net increase in λ with increasing temperature, there are competing effects between the explicit and implicit temperature dependence in Eq. (3.3). The former clearly increases λ while the latter

decreases λ (the ratio of Fermi functions in Eq. (3.3) goes to 1 for $\eta \ll -1$ and increase linearly with η for $\eta \gg 1$).

The increases in absorption by the reduced electron degeneracy follow from the thermal average. Consider the weighting function in Eq. (2.1.1),

$$
\begin{aligned}
G_\eta(u) &= \frac{\sqrt{\pi}}{2I_{1/2}(\eta)} \int_o^\infty dx\, f_\eta(x)\big[1 - f_\eta(x+u)\big] \\
&= \frac{\sqrt{\pi}}{2(1-e^{-u})I_{1/2}(\eta)} \ln\left\{\frac{1+e^\eta}{1+e^{\eta-u}}\right\}
\end{aligned}
\tag{4.2.1}
$$

The range of integration in Eq. (4.2.1) is controlled by the degeneracy. The extreme degeneracy limit clearly shows this effect where $G_\eta(u)$ increases linearly with $u = \hbar\omega/T$ until $u = \eta$ at which point it becomes constant. Table 1 shows the decrease in electron degeneracy with rising temperature and consequent increase in $G_\eta(u)$ for $\hbar\omega = 30\,eV$.

Displayed in Fig. 4 are calculations of $\nu(\omega)$ for solid-density Al at $T = 0.025$ and $10\,eV$. To estimate the separate impact of the two effects (increased λ and decreased η) a calculation at $T = 10\,eV$ using the same effective electron-ion interaction as the cold case (i.e.; artificially adjust the screening length to the cold result) is also displayed. The figure shows the largest increase in $\nu(\omega)$ from reduced degeneracy at small ω, which is expected since the smaller the photon energy the more degeneracy restricts the available final states. The increase from a larger λ is approximately ω independent.

Also displayed in Fig. 4 is the Born approximation to the collision frequency using Eq. (2.3.4). It considerably overestimates the all-order calculations for either $T = 0.025$ or $10\,eV$. Furthermore, the Born results underestimate the temperature dependence of $\nu(\omega)$. Clearly, weak-scattering theory fails for the electron-ion interaction in the present model.

4.3 Cold Li and Na

Although Al is the prototypical simple metal with tightly bound, weakly polarizable core electrons, the model can be readily applied to other elements and conditions since the input is an effective electron-ion interaction defined by the material conditions. In Fig. 5 comparisons are made to solid Li and Na experimental data. [14] The frozen core interaction has the same functional form as in Eq. (4.1) except that the fitting parameters reproduce atomic data for the

valence electron in neutral Li and Na [12] and the screening length is adjusted to the appropriate free electron density. The figure shows reasonable agreement of the present model with experimental data for Li and Na for $\omega > \omega_p$.

5. Approximations

Although the reasonable agreement with the cold experimental data is tantalizing, the present model makes several *ad hoc* approximations. It is possible, however, to estimate errors due to several neglected or approximated physical processes.

5.1 Electron screening

The present model not only neglects dynamic screening, but it also assumes an exponentially decaying interaction. To test the approximation, the thermally averaged collision frequency calculations using $g^{(2)}(\varepsilon,\omega)$ in Eq. (2.3.1) with $S(q) = 1$ and a Coulomb potential screened by the RPA $D(q,\omega)$ are compared to calculations with $g^{\lambda}_{Born}(\varepsilon,\omega)$ in Eq. (2.3.5). In addition, the results using $g^{\lambda}_{Born}(\varepsilon,\omega)$ are corrected by the index of refraction to account for dispersive behavior present in $D(q,\omega)$. Their ratio is plotted in Fig. 6 for solid-density Al at $T = 0.1 eV$ showing that for $\omega > \omega_p$ the static approximation and dynamic screening agree reasonably well.

5.2 Ion-ion correlations

A neglected process in the present model is the interference of scattered waves from nearby ions. This phenomenon can be readily included through the ion structure factor in the Born approximation. [5-8] To estimate their impact, the collision frequency is computed in the Born approximation using the static screening length in Eq. (3.3) with an approximation for $S(q)$. The structure factor was obtained using the Percus-Yevick equation for hard-spheres [22,23] with a packing fraction of 0.45. [24] The ratio of the results with and without ion-ion correlations for solid-density Al at $T = 0.1 eV$ is plotted in Fig. 6 showing ~10% correction over the photon energies of interest. Increasing the ion temperature leads to broadening of the features in $S(q)$ [24] further reducing the importance of ion correlations.

The small impact of ion-ion correlations on the collision frequency for $\omega > \omega_p$ follows from the limits on the momentum transfer integration. For example, at high degeneracy the thermal average in Eq. (2.1.1) is weighted towards values near the chemical potential. Assuming Al at

solid density and $T = 0.1 eV$, then for $\varepsilon = \eta T \approx 12 eV$ and $\hbar \omega = \hbar \omega_p \approx 15 eV$ the limits of integration in Eq. (2.3.1) are

$$k_- \approx 0.94 \mathring{A}^{-1} \quad \text{and} \quad k_+ \approx 4.5 \mathring{A}^{-1} \tag{5.2.1}$$

This range encompasses the first peak and part of the second in the structure factor. [24] Consequently, for $\omega > \omega_p$ ion-ion correlations should not significantly affect the photon absorption. Conversely, for $\omega \le \omega_p$ the ion-ion correlations would impact the results.

5.3 Frozen-core potential

The model assumes a frozen core potential to describe the localized bound electrons. At small frequencies the polarization of the bound electrons is negligible. At higher photon energies, however, the dynamic response of the core can become important. [19] That is, the assumed core potential is adequate to describe electron scattering from Al^{+3} at large impact parameters, but it is only approximate for the core penetrating collisions required for absorption at photon energies approaching the ionization of the L-shell electrons.

The relative contribution of the frozen-core potential is displayed in Fig. 1 by an absorption calculation using the present model but setting $V_b(r) = 0$ that shows considerable larger disagreement with the experimental data than the full potential result. The discrepancy between the present model and experimental data together with the model variation when setting $V_b(r) = 0$ suggest that simulating the dynamic response of the bound electrons in the present model could improve the agreement with the cold experimental data. [19]

6. Vinko et al model [1] (VGW)

Recently VGW proposed a semi-analytical photon absorption model for plasmas and simple metals to study warm dense matter, but their results differ from the present effort. Briefly, the VGW model is a weak-scattering approximation with thermal average in Eq. (2.1.1) corrected for stimulated emission (see Appendix). Their calculations used a pseudo-potential together with the RPA or a local field corrected (LFC) dielectric function as well as an ion structure factor for the crystal or one suitable for liquids. [1]

Their results [1] are displayed in Fig. 1. As discuss in VGW, the molecular dynamics simulation (MD) agree with the cold experimental data (also with the present model) only at low frequencies where the neglected particle-hole interactions in the MD simulations are small. The VGW-RPA semi-analytic model and MD results agree for $\omega \ge 15 eV$ (limit of available VGW

semi-analytical model calculations) and there is significant improvement compared to the measurements using the VGW-LFC dielectric function.

6.1 Pseudo-potential

The electron-ion interaction in VGW is the empty-core potential with Fourier transform

$$\tilde{V}(q;R_c) = -4\pi Ze^2 \cos(qR_c)/q^2 \tag{6.1.1}$$

where R_c is a free parameter determined by fitting a property of the solid. Their choice of $R_c = 0.6\text{Å}$ was based on reproducing Fermi surface measurements. [1] Interestingly, the value for R_c can vary by about a factor of 2 depending on the fitted physical quantity. [25] The sensitivity of the absorption model to R_c was not addressed by VGW.

There is reason for skepticism regarding the reported [1] improved agreement between the cold, solid Al experimental data and the VGW-LFC model. Specifically, the statically screened pseudo-potential, $\tilde{V}(q;R_c)/D(q,\omega=0)$, is used to determine R_c when fitting the Fermi surface eigenvalues. [25] It appears, however, that VGW set $R_c = 0.6\text{Å}$ in all their absorption calculations independent of the different dielectric function approximations.

The possible consequences of this inconsistency are examined using a simplified procedure. The value $R_c = 0.6\text{Å}$ is retained for the RPA dielectric function as in VGW. To determine R_c for the LFC dielectric function, the thermally averaged collision frequency at $\omega=0$ for cold, solid Al is fitted to the RPA result. These calculations use Eq. (2.3.1) with the degeneracy parameter in Table 1, $S(q)=1$, and screening approximated by

$$\underset{q\to 0}{Lim}\,\frac{\tilde{V}(q;R_c)}{D(q,\omega=0)} = -\frac{4\pi Ze^2\lambda^2}{1+\lambda^2 q^2}\cos(qR_c) \tag{6.1.2}$$

For the RPA dielectric function

$$\lambda \to \lambda_{TF} = \sqrt{\pi a_o/4k_F} \tag{6.1.3}$$

where $k_F = \left(3\pi^2 n_e\right)^{1/3}$ defines the Fermi wave number and λ_{TF} is the Thomas-Fermi screening length. For the Hubbard [25,26] local field corrected dielectric function (HLFC)

$$\lambda \to \lambda_H = \lambda_{TF}\sqrt{1-\frac{\kappa}{4k_F^2\lambda_{TF}^2}} \tag{6.1.4}$$

where $\kappa = 1+0.158/\pi k_F a_o$ chosen to satisfy the compressibility sum rule. The procedure yields $R_c = 0.745\text{Å}$ for the HLFC dielectric function.

Although this approach does not follow VGW, it is comparable and consistent. The pseudo-potentials idea is to approximate the wavefunction in the region outside the atomic core with a weaker potential that it is hoped suitable for perturbation theory. When fitted to the eigenvalues, the quasi-particle structure near the Fermi surface is optimized. [25] Similarly, the collision frequency at $\omega = 0$ is determined by the phase-shifts at energies near the Fermi surface. [3]

Calculations of the thermally averaged collision frequency for cold, solid Al are compared in Fig. 7. All these calculations use Eq. (2.3.1) with $S(q) = 1$ and static screening of $\tilde{V}(q;R_c)$ described by λ_{TF} or λ_H). In addition, the HLFC calculations in the figure are normalized to the RPA results. It follows that the HLFC calculations using $R_c = 0.6\mathring{A}$ are 50-100% greater than the RPA results; compatible with the enhancement reported by VGW. On the other hand, the HLFC calculations with $R_c = 0.745\mathring{A}$ are about the same as the RPA results for $\hbar\omega < 50\,eV$. Thus, a consistent treatment of the pseudo-potential may well impact the conclusions in VGW.

6.2 Temperature dependence

The temperature dependence of the solid-density Al absorption at constant photon energy in Fig. 8 shows different behaviors from VGW-LFC and the present model. To emphasize the temperature dependence, each calculation in Fig. 8 was normalized to its respective value at room temperature. In an effort to ascertain the source of the discrepancy, additional calculations using the following expressions are displayed in Fig. 8,

$$\left.\begin{array}{c} \alpha_1(\omega) \\ \\ \alpha_2(\omega) \end{array}\right\} = \left(1 - e^{-\hbar\omega/T}\right)\frac{\omega_p^2}{\omega^2 c}\left\{\begin{array}{c} \nu(\omega) \\ \\ \nu_{Born}(\omega) \end{array}\right. \tag{6.2.1}$$

That is, both compute the collision frequency using the electron-ion interaction from the present model and both neglect dispersion and multiple collisions. The difference is that $\alpha_1(\omega)$ is all-order in the interaction while $\alpha_2(\omega)$ makes the Born approximation. The similarities between $\alpha_1(\omega)$ and the present model in Fig. 7 show that dispersion and multiple collisions have, as expected, [7] small impact well above the plasma frequency. The similarities between $\tilde{\alpha}_2(\omega)$ and VGW-LFC suggest that the weak-scattering approximation is the source of the discrepancy.

7. Conclusion

A relatively straightforward model for the photon absorption of plasmas and simple metals was proposed. The approach is based on a Drude picture where the electron-ion collision

frequency is obtained from the usual inverse bremsstrahlung all-order formula corrected for degeneracy and many-body screening. The results are in reasonable agreement with the cold, solid Al measurements of the photon absorption and index of refraction. The contribution of the atomic core portion of the electron-ion interaction to the model absorption is found to be significant as well as necessary to attain reasonable agreement with the experimental data. Furthermore, it is possible that the neglected dynamic response of the bound electrons (frozen-core approximation) is partly responsible for residual errors.

The model displayed, in agreement with physical intuition, an enhancement in the XUV absorption as the rising temperature increases the many-body screening length and reduces electron degeneracy. As expected, [5,7,8] estimates of ion-ion correlations and dynamic screening effects produced only small corrections to the XUV absorption.

It was found that the Born approximation overestimates the all-order calculation for the collision frequency by more than an order of magnitude and underestimates the temperature dependence. Furthermore, numerical tests suggest that the discrepancies in the absorption temperature behavior between the present model and that proposed by Vinko et al [1] is due to the weak-scattering approximation in the latter.

The proposed model is not specific to solid density Al. The only input is a semi-analytical electron-ion interaction, which is defined by the material conditions. Consequently, the model can be readily applied to other conditions with appropriate changes in the interaction. For example, the model was in reasonable agreement with cold, solid Li and Na experimental absorption data and was implemented in the OPAL and TOPAZ opacity codes. [27-29] Finally, experimental determination of the photon absorption, specifically the temperature dependence of XUV absorption by solid-density Al, should enhance the fundamental understanding of warm dense matter and help resolve existing theoretical discrepancies.

APPENDIX

Ron-Tzoar [6] and Born approximation

Ron and Tzoar give the absorption extinction coefficient for a plasma or simple metal in the form [1,6]

$$\alpha(\omega) = \frac{n}{6\pi^2 m^2 \omega^3 c} \int_o^\infty dq\, q^6 \frac{\tilde{V}^2(q)}{|D(q,\omega)|^2} S(q) \text{Im}\{D(q,\omega) - D(q,0)\} \tag{A.1}$$

This expression can be rewritten using the dielectric function [6]

$$D(q,\omega) = 2\int \frac{d\vec{p}}{(2\pi)^3} \frac{n_{|\vec{p}|} - n_{|\vec{p}+\vec{q}|}}{\hbar\omega + E_{|\vec{p}|} - E_{|\vec{p}+\vec{q}|} + i\xi}$$

$$= 2\int \frac{d\vec{p}}{(2\pi)^3} \frac{n_{|\vec{p}-\vec{q}/2|} - n_{|\vec{p}+\vec{q}/2|}}{\hbar\omega - \hbar^2 \vec{p}\cdot\vec{q}/m + i\xi} \tag{A.2}$$

where the second line involves a change of variables and analytic continuation has $\xi \to 0^+$,

$$\alpha(\omega) = \frac{ne^2}{3\pi^2 m^2 \omega^3 c} \int d\vec{p} \int_o^\infty dq\, q^4 \frac{\tilde{V}^2(q)}{|D(q,\omega)|^2} S(q) \left\{ n_{|\vec{p}-\vec{q}/2|} - n_{|\vec{p}+\vec{q}/2|} \right\} \delta\left(\hbar\omega - \frac{\hbar^2}{m}\vec{p}\cdot\vec{q}\right) \tag{A.3}$$

The one-electron Fermi distribution and energy are, respectively,

$$n_p = f_\eta\left(\frac{E_p}{T}\right) \tag{A.4}$$

with $f_\eta(x)$ in Eq. (2.1.2) and

$$E_p = \frac{\hbar^2 p^2}{2m} \tag{A.5}$$

To proceed, use the energy conserving delta-function in Eq. (A.3) to write,

$$n_{|\vec{p}-\vec{q}/2|} - n_{|\vec{p}+\vec{q}/2|} = \left(1 - e^{-\hbar\omega/T}\right) n_{|\vec{p}-\vec{q}/2|} \left(1 - n_{|\vec{p}+\vec{q}/2|}\right) \tag{A.6}$$

Then, substituting Eq. (A.6) into Eq. (A.3), performing the solid angle integration, changing variables $\vec{p} = \vec{p} + \vec{q}/2$, and introducing $x = \hbar^2 p^2/2mT$ and $u = \hbar\omega/T$, yields

$$\alpha(\omega) = \frac{16ne^6}{3\hbar^4\omega^3 c}\left(1 - e^{-u}\right)\int_o^\infty dx\, f_\eta(x)\left[1 - f_\eta(x + u)\right]\int_{k_-}^{k_+} \frac{dq}{q} S(q)\frac{F^2(q)}{\left|D(q,\omega)\right|^2} \tag{A.7}$$

with $F(q)$ and $k_\pm$ defined in Eqs. (2.3.2) and (2.3.3). The second-order expression in Eq. (A.7) explicitly displays the stimulated emission correction and the thermal average over initial particle plus final holes and is identical to the Born approximation from the "inverse bremsstrahlung" approach. [5,7,8]

References

[1] S.M. Vinko *et al*, *HEDP* **5** (2009) 124.

[2] H. Reinholz *et al*, *Phys.Rev.* **E62** (2002) 5648; *and references therein*

[3] R.R. Johnston, *JQSRT* **7** (1967) 815

[4] H.A. Kramers, *Phi.Mag.* **46** (1923) 836

[5] J. Dawson & C. Oberman, *Phys.Fluids* **5** (1962) 517; *ibid*, **6** (1963) 394

[6] A. Ron & N. Tzoar, *Phys.Rev.* **131** (1963) 12

[7] G. Bekefi, *Radiation Processes in Plasmas* (Wiley and Sons, New York, 1966)

[8] M. Nakagawa, Y. Kohyama & N Itoh, *Ap.J.Suppl.* **63** (1987) 661

[9] Abramowitz, M. & Stegun, L.A. 1972, *Handbook of Mathematical Functions* (National Bureau of Standards, Washington, D.C.)

[10] J.M Ziman, *Principles of the Theory of Solids* (Cambridge University Press, 1964)

[11] Ya.B. Zel'dovich & Yu.P. Raizer, *Physics of Shock Waves and High Temperature Hydrodynamic Phenomena* (Academic Press, N.Y., 1967, Vol. 1, pg. 257.

[12] F.J Rogers, B.G. Wilson & C.A. Iglesias, *Phys.Rev.* **A38** (1988) 5007.

[13] H.J. DeWitt, *J.Nucl.Energy* **C2** (1961) 27

[14] B.L. Henke, E.M. Gullikson & J.C. Davis, *Atomic Data & Nuclear Data* **54** (1993) 181

[15] E.M. Gullikson, P. Denham, S. Mrowka & J.H. Underwood, *Phys.Rev.* **B49** (1994) 16283

[16] R. Keenan, C. Lewis, J. Wark & E. Wolfrum, *J.Phys.* **B35** (2002) L447

[17] B.G. Wilson, MH. Chen & C.A. Iglesias, *JQSRT* **81** (2003) 499.

[18] J. Green, BREMII - *A code for calculating free-free Gaunt factors in an arbitrary potential*, Report RDA-TR-237AEC, R&D Associates, Santa Monica, CA, 1973

[19] K. Sturm, E. Zaremba & K. Nuroh, *Phys.Rev.* **B42** (1990) 6973

[20] D.B. Tanner, A.J. Sievers & R.A. Buhrman, *Phys.Rev.* **B11** (1975) 1330

[21] E.M. Gullikson, web site *X-Ray Interaction with Matter*, http://henke.lbl.gov/optical_constants/

[22] E. Thiele, *J.Chem.Phys.* **39** (1963) 474

[23] M.S. Wertheim, *Phys.Rev.Lett.* **10** (1963) 321

[24] J.M. Stallard & C.M. Davis, Jr., *Phys.Rev.* **A8** (1973) 368

[25] A.P. Horsfield & N.W. Ashcroft, *J.Phys Condens. Matter* **5** (1993) 3925

[26] J. Hubbard, *Proc.Roy.Soc.* **A243** (1957) 336

[27] C.A. Iglesias & F.J. Rogers, *Ap.J.* **464** (1996) 943

[28] C.A. Iglesias & S.J. Rose, *Ap.J. Letters* **466** (1996) L115

[29] C.A. Iglesias *et al*, *JQSRT* **81** (2003) 227

TABLE 1

Degeneracy from Eq. (3.4), screening parameter, and value of $G_\eta(u)$ at $\hbar\omega = 30eV$ for solid-

density Al at several temperatures.

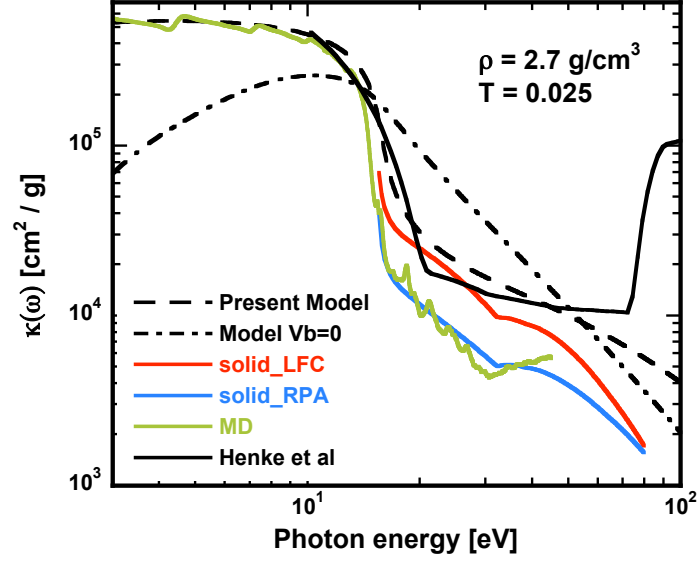| T [eV]	η	$\lambda[a_o]$	$G_\eta(u)$
0.025	467.2	0.918	0.0547
0.1	115.9	0.923	0.109
1	11.58	0.924	0.343
2	5.676	0.934	0.476
4	2.579	0.981	0.627
7	1.038	1.088	0.725
10	0.2745	1.204	0.765

FIGURE CAPTIONS

Fig. 1 Photon absorption cross-section versus photon energy for cold, solid Al from several models compared to experimental data [14] with L-edge at $\hbar\omega \approx 73\,eV$.

Fig. 2 Index of refraction versus photon energy for solid-density Al: present model at $T = 0.025\,eV$ (*solid*) and $T = 10\,eV$ (*short-dash*), cold experimental data (*circles*), [20,21] and collisionless limit $n_o(\omega)$ (*long-dash*).

Fig. 3 Ratio of absorption for solid-density Al versus photon energy from present model at various temperatures to the $T = 0.025\,eV$ result.

Fig. 4 Thermally averaged collision frequency versus photon energy from present model using all-order and Born approximation for solid-density Al at $T = 0.025$ and $10\,eV$. Also, all-order calculations for $T = 10\,eV$ with λ corresponding to the $T = 0.025\,eV$ value.

Fig. 5 Photon absorption cross-section versus photon energy for cold, solid Li and Na from present model (*solid*) and experimental data (*circles*). [14] The data is not plotted beyond the first photon ionization threshold.

Fig. 6 Ratio of thermally averaged electron-ion collision frequency versus photon energy for solid-density Al at $T = 0.1\,eV$: Born approximation with dynamic and static screening (*solid*); Born approximation with hard-sphere $S(q)$ and $S(q) = 1$ (*dot-dash*); all-order calculation with $V_b(r)$ in Eq. (4.1) and $V_b(r) = 0$ (*dash*).

Fig. 7 Thermally averaged collision frequency using HLFC statically screened pseudo-potential: $R_c = 0.745\,\text{Å}$ (*solid*) and $R_c = 0.6\,\text{Å}$ (*dash*). The results are normalized to the RPA statically screened pseudo-potential with $R_c = 0.6\,\text{Å}$.

Fig. 8 Photon absorption for solid-density Al at $\hbar\omega = 30\,eV$ as a function of temperature: Present model (*solid*), $\alpha_1(\omega)$ (*dot-dash*), $\alpha_2(\omega)$ (*short-dash*), and VGW-LFC [1] (*long-dash*). Each calculation is normalized to their respective $T = 0.025\,eV$ value.

Fig. 1 Photon absorption cross-section versus photon energy for cold, solid Al from several models compared to experimental data [14] with L-edge at $\hbar\omega \approx 73\,eV$.
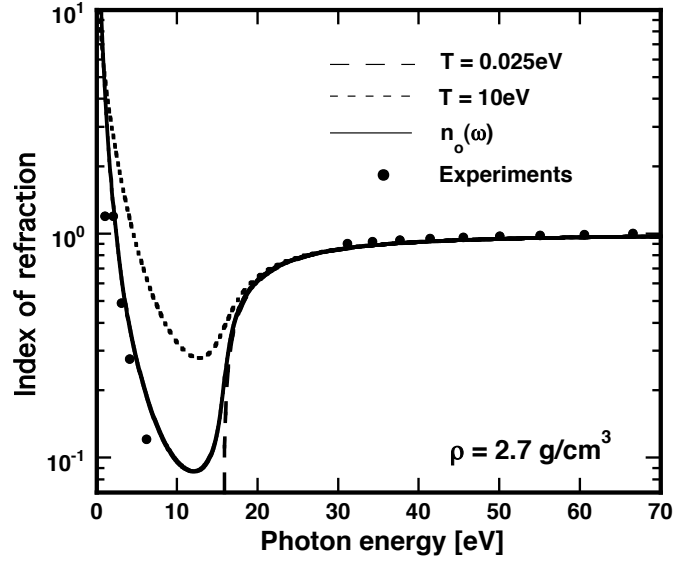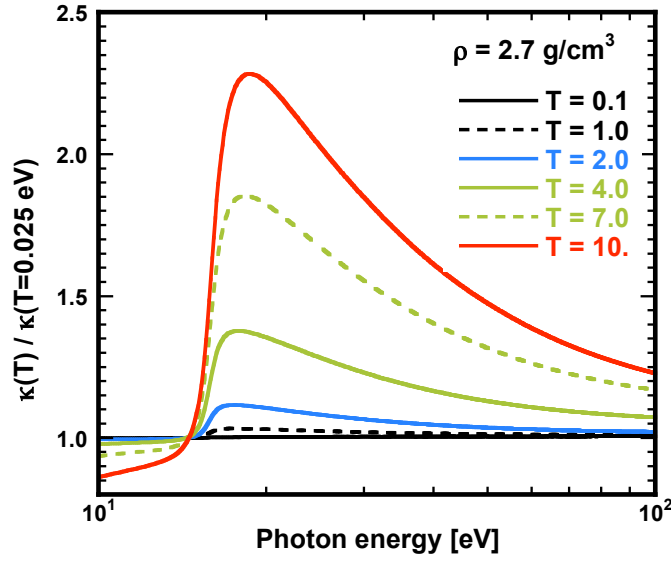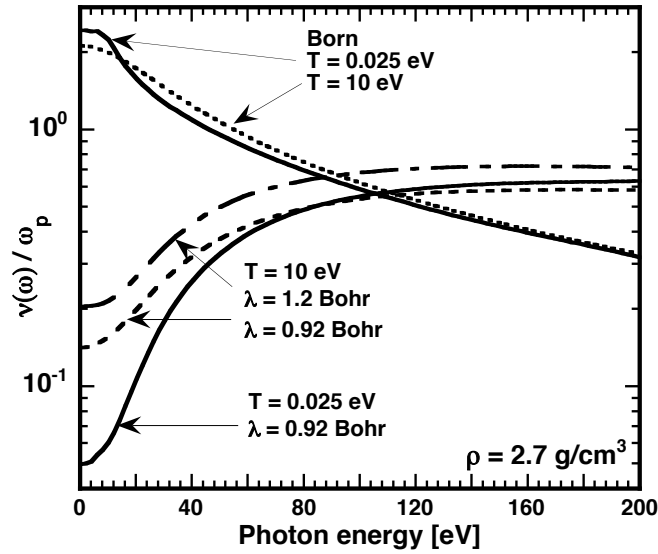

Fig. 2 Index of refraction versus photon energy for solid-density Al: present model at $T = 0.025\,eV$ (*solid*) and $T = 10\,eV$ (*short-dash*), experimental data at $T = 0.025\,eV$ (*circles*), [20,21] and collisionless limit $n_o(\omega)$ (*long-dash*).

Fig. 3 Ratio of absorption for solid-density Al versus photon energy from present model at various temperatures to the $T = 0.025\,eV$ result.

Fig. 4 Thermally averaged collision frequency versus photon energy from present model using all-order and Born approximation for solid-density Al at $T = 0.025$ and $10\,eV$. Also, all-order calculations for $T = 10\,eV$ with λ corresponding to the $T = 0.025\,eV$ value.
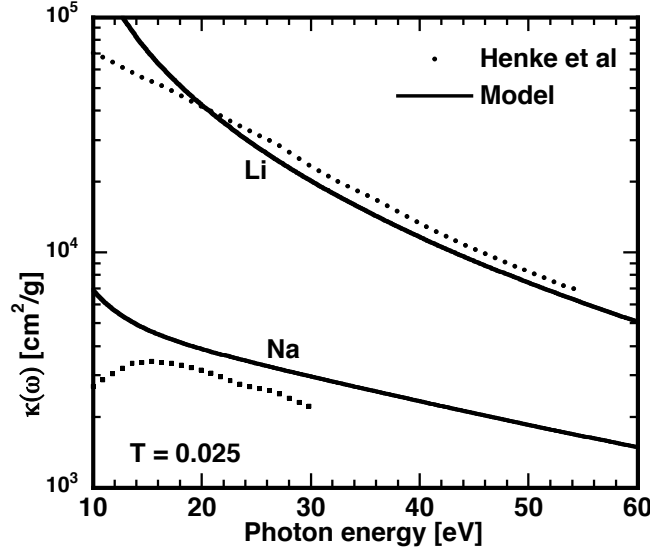
Fig. 5 Photon absorption cross-section versus photon energy for cold, solid Li and Na from present model (*solid*) and experimental data (*circles*). [14] The data is not plotted beyond the first photon ionization threshold.
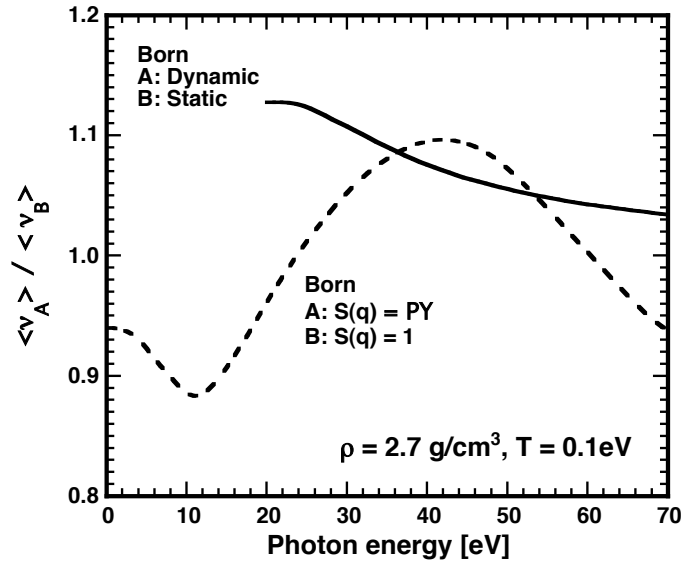

Fig. 6 Ratio of thermally averaged electron-ion collision frequency versus photon energy for solid-density Al at $T = 0.1eV$: Born approximation with dynamic and static screening (*solid*); Born approximation with hard-sphere $S(q)$ and $S(q) = 1$ (*dot-dash*); all-order calculation with $V_b(r)$ in Eq. (4.1) and $V_b(r) = 0$ (*dash*).
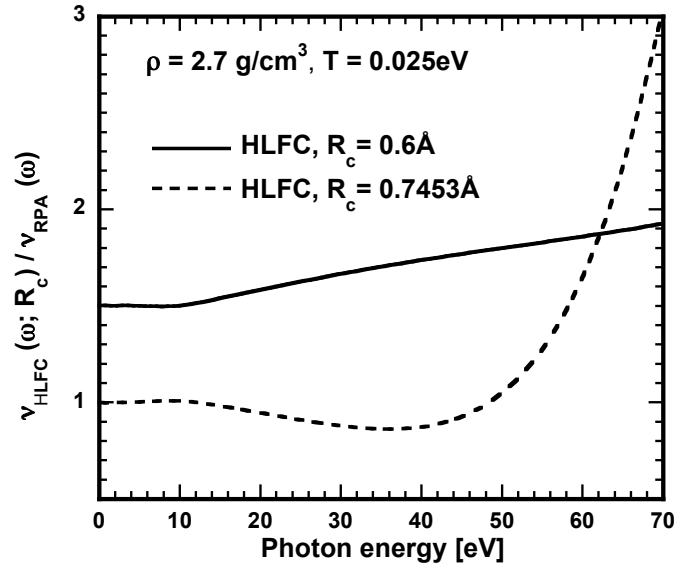
Fig. 7 Thermally averaged collision frequency using HLFC statically screened pseudo-potential: $R_c = 0.745\,\text{Å}$ (*solid*) and $R_c = 0.6\,\text{Å}$ (*dash*). The results are normalized to the RPA statically screened pseudo-potential with $R_c = 0.6\,\text{Å}$.
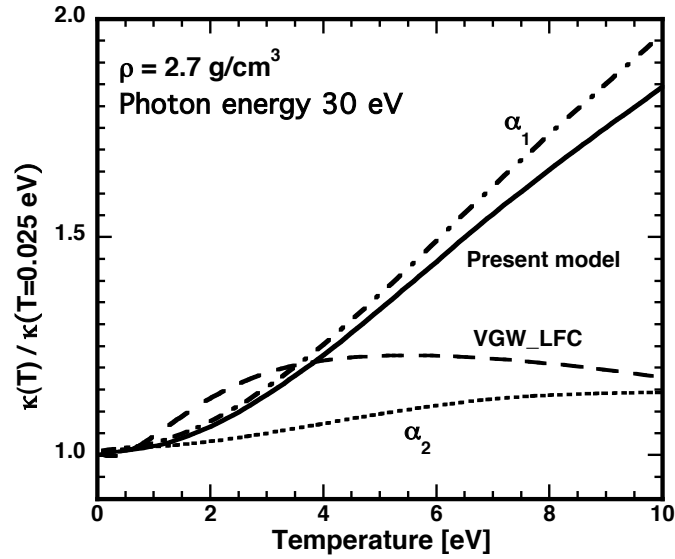

Fig. 8 Photon absorption for solid-density Al at $\hbar\omega = 30eV$ as a function of temperature: Present model (*solid*), $\alpha_1(\omega)$ (*dot-dash*), $\alpha_2(\omega)$ (short-*dash*), and VGW-LFC [1] (*long-dash*). Each calculation is normalized to their respective $T = 0.025eV$ value.